THE JOURNAL OF PHYSICAL CHEMISTRY B

ARTICLE

pubs.acs.org/JPCB

Nonadiabatic Excited-State Molecular Dynamics Modeling of Photoinduced Dynamics in Conjugated Molecules

Tammie Nelson,[†] Sebastian Fernandez-Alberti,[‡] Vladimir Chernyak,[§] Adrian E. Roitberg,[∥] and Sergei Tretiak*,[†]

[†]Theoretical Division, Center for Nonlinear Studies (CNLS), and Center for Integrated Nanotechnologies (CINT), Los Alamos National Laboratory, Los Alamos, New Mexico 87545, United States

[‡]Universidad Nacional de Quilmes, Roque Saenz Peña 352, B1876BXD Bernal, Argentina

[§]Department of Chemistry, Wayne State University, 5101 Cass Avenue, Detroit, Michigan 48202, United States

[∥]Departments of Physics and Chemistry, Quantum Theory Project, University of Florida, Gainesville, Florida 32611, United States

ABSTRACT: Nonadiabatic dynamics generally defines the entire evolution of electronic excitations in optically active molecular materials. It is commonly associated with a number of fundamental and complex processes such as intraband relaxation, energy transfer, and light harvesting influenced by the spatial evolution of excitations and transformation of photoexcitation energy into electrical energy via charge separation (e.g., charge injection at interfaces). To treat ultrafast excited-state dynamics and exciton/charge transport we have developed a nonadiabatic excited-state molecular dynamics (NA-ESMD) framework incorporating quantum transitions. Our calculations rely on the use of the Collective Electronic Oscillator (CEO) package accounting for many-body effects and actual potential energy surfaces of the excited states combined with Tully's fewest switches algorithm for surface hopping for probing nonadiabatic processes. This method is applied to model the photoinduced dynamics of distyrylbenzene (a small oligomer of polyphenylene vinylene, PPV). Our analysis shows intricate details of photoinduced vibronic relaxation and identifies specific slow and fast nuclear motions that are strongly coupled to the electronic degrees of freedom, namely, torsion and bond length alternation, respectively. Nonadiabatic relaxation of the highly excited mA_g state is predicted to occur on a femtosecond time scale at room temperature and on a picosecond time scale at low temperature.

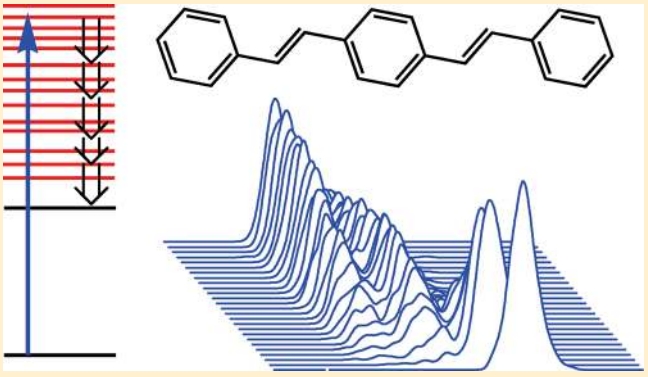

I. INTRODUCTION

Many nanoscale materials have already found applications or have great technological potentials for photovoltaics,[1−4] light emitting devices,[5−7] and biosensors,[8−10] to name a few. Frequently, understanding their complex electronic dynamics[11,12] is the main challenge for applications, particularly in the realm of energy-related research. For example, many of the unique electronic and photophysical properties of organic conjugated molecules arise from the highly polarizable and delocalized π-electron system which supports mobile charge carriers.[13,14] Systems such as conjugated polymers and dendrimers exhibit efficient light harvesting over a broad range of the solar spectrum.[15−17] Consequently, in recent years, conjugated polymers have offered a new design for photovoltaics due to their ability to generate electrical current upon light absorption.[18,19] Conjugated polymers can also emit light, the color of which can be fine-tuned by adjusting the chemical structure.[20−22] Organic light-emitting diodes are already used in commercially available display technology. In addition, various applications of conjugated polymers have been proposed ranging from transistors[23,24] and electrochemical cells[22] to chemical and biological sensors[9,25] and imaging devices.[26,27]

Unlike traditional semiconductors, conjugated polymers feature a large electron−vibrational coupling due to their relatively soft molecular structure and large exciton binding energy owing to low dimensionality and low dielectric constant.[28−30] Understanding the photoexcitation dynamics in such materials is vital to providing an accurate description of photophysical processes such as exciton formation, evolution, and decay via nonadiabatic (NA) dynamics. Nonadiabatic dynamics can lead to charge or energy transfer and to nonradiative relaxation to the ground or low lying excited states. Sophisticated modeling of nanometer

Special Issue: Shaul Mukamel Festschrift

Received: October 4, 2010
Revised: November 22, 2010
Published: January 10, 2011

length scale and subnanosecond time scale dynamics of excited electron−vibrational states is computationally demanding. Not only should the ground many-electron state be calculated on the fly as the nuclear trajectories evolve, but also optically accessible excited states should be found. Some success has recently been achieved for the adiabatic (Born−Oppenheimer, BO) molecular dynamics propagating the trajectory along the ground[31] or excited-state molecular potential energy surfaces (PES).[28,32,33] The previously developed semiempirical excited-state molecular dynamics (ESMD) approach allows us to follow the ultrafast dynamics on femtosecond to nanosecond time scales in large organic molecules.[29,34,35] Similar methodologies currently exist for density functional theory (DFT) and time-dependent DFT (TDDFT) frameworks.

The situation is even more complex when the electronic and nuclear dynamics become nonadiabatic and show quantum mechanical features in the vicinity of the level crossing (electronic state degeneracy).[36−39] Straightforward quantum mechanical simulations in such cases are not feasible. Semiclassical methods for numerical studies of quantum effects in systems with a large number of nuclear degrees of freedom have been developed based on path-integral techniques[40,41] and simultaneous solution of nuclear dynamics and electronic structure problems in the ab initio multiple spawning (AIMS) method[36,38,42] or using a model Hamiltonian for quantum dynamics with the computationally demanding multiconfigurational time-dependent Hartree (MCTDH) method to solve the time evolution of the nuclear wave packet.[43−45]

Molecular dynamics with quantum transitions (MDQT) is another well tested and computationally tractable method for the simulation of nonadiabatic dynamics. In particular, the fewest switches surface hopping (FSSH) scheme described by Tully[46] includes an "on the fly" calculation of the excited-state surfaces and electronic couplings. In the surface hopping method, the nuclei are treated classically, while the electrons are treated within the quantum mechanical framework. At any given time, the nuclei are evolved on a single adiabatic potential energy surface, and the system is allowed to transition between electronic states depending on the strength of the nonadiabatic coupling.[47] FSSH is one of the most popular alternatives to Ehrenfest dynamics[48] due to its simplicity and accuracy, and it reliably provides statistically correct electronic state populations in a Monte Carlo sense. The FSSH approach combined with semiempirical model Hamiltonian and multireference configuration interaction (MR-CI) has been successfully applied to model photoinduced dynamics in small molecules and nonradiative relaxation in DNA bases.[49−52] To keep the FSSH routines numerically tractable for large molecular systems, a series of approximations have been made to lighten the computational load.[47,51,53−55] The most severe is the Classical Path Approximation which assumes that nuclear dynamics is independent of electronic evolution; in this case, a single ground-state trajectory is used as input for the nonadiabatic simulations. Another drastic approximation is the neglect of electronic correlations so that the excited states are described as single-electron excitations. In this framework, recent time-domain DFT simulations have shown the importance of nonadiabatic effects in photodynamics and have provided a number of valuable insights into several classes of electronic materials.[54−57] However, such approximations may not be suitable for organic conjugated molecular materials featuring collective many-body effects and large electron−phonon couplings.

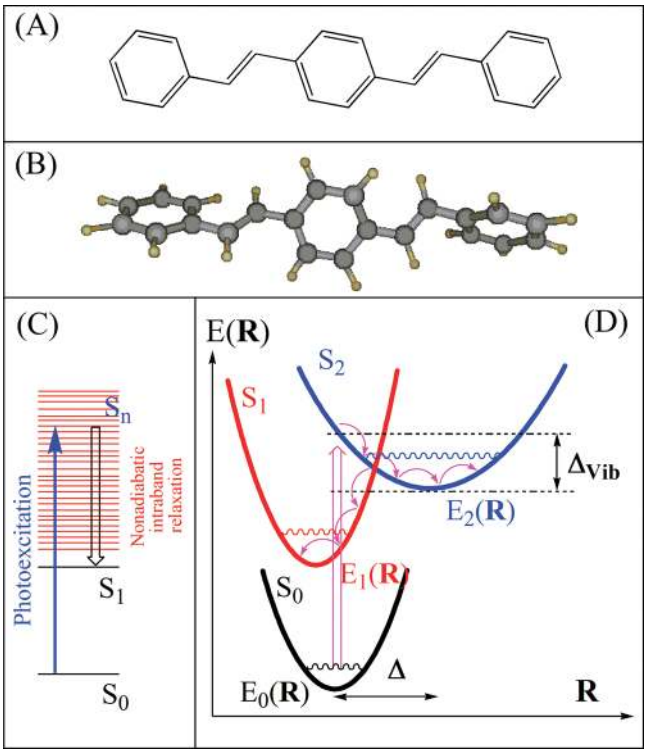

Figure 1. (A) Distyrylbenzene chemical structure and (B) a snapshot from the ground-state trajectory revealing the geometry conformations. (C) Schematic representation of molecular photoexcitation and intraband relaxation (internal conversion) via nonadiabatic vibronic dynamics. (D) Schematic representation of MDQT dynamics. The excited-state energy E_α is a function of the nuclear coordinates **R**. The nuclear trajectory is propagated on the excited-state Born−Oppenheimer potential energy surface, and transitions between electronic states are allowed.

In this study, we present a theoretical methodology extending the ESMD framework to incorporate nonadiabatic quantum transitions based on the FSSH scheme.[46] This method partially addresses the drawbacks described above, while remaining numerically tractable. The configuration interaction singles (CIS) or time-dependent Hartree−Fock (TDHF) formalism combined with the semiempirical model Hamiltonian serves as a numerically efficient technique for computing excited states in large systems. The TDHF approach incorporates essential electronic correlations present in the excited states of molecular materials such as excitons. The Langevin thermostat accounts for simple thermal bath effects.[58] Calculations of the excited-state gradients and nonadiabatic couplings *analytically* allow propagation of the trajectory along the excited-state potential energy surface "on the fly". Consequently, the NA-ESMD methodology will allow nonadiabatic dynamics simulation (such as intraband relaxation, Figure 1) of molecular systems with hundreds of atoms and on ∼10 ps time scales. From these calculations, we can learn about energy (vibrational and electronic) relaxation and transfer rates, details of the nonadiabatic couplings and their relationship with molecular motion, and spectroscopy signatures. Trial applications of this methodology using numerical derivatives for nonadiabatic couplings uncovered intricate details of photoinduced ultrafast energy transfer in small conjugated dendrites.[59,60] Here we further demonstrate the use of this technique to model the photoinduced dynamics of distyrylbenzene (a small oligomer of polyphenylene vinylene, PPV) focusing on the

nonradiative relaxation of the mA_g excited state to the lowest singlet excited $1B_u$ state, which plays an important role in absorption, photoluminescence, and carrier transport in conjugated systems. PPV is among the most promising organic conjugated polymers for use in optoelectronic devices due to its unique electronic and optical properties and synthetic flexibility.[61−63]

Section II describes in detail the NA-ESMD theoretical approach used in our simulations and discusses numerical implementation of the surface hopping methodology. In Section III, we present the results of our numerical simulations of photoexcited dynamics in distyrylbenzene including a detailed analysis of population decay time scales, wavepacket evolution, vibrational coordinates coupled to the excitation dynamics, and their PES. Finally, we summarize our findings in Section IV.

II. THEORETICAL METHODOLOGY

A. Computation of Excited States. Over the years, Mukamel and co-workers have developed an efficient collective electronic oscillator (CEO) approach[64,65] for excited-state calculations. The CEO code is based on the well-tested major semiempirical models (such as AM1, PM1, INDO, INDO/S, etc.)[66,67] combined with a time-dependent Hartree−Fock (TDHF) or configuration interaction singles (CIS) formalism.[68] The CEO approach solves the TDHF equation of motion[68] for the single-electron density matrix[69] of a molecule driven by an external electric field

$$\rho_{mn}(t) = \langle \Psi(t)|c_m^\dagger c_n|\Psi(t)\rangle \tag{1}$$

where $|\Psi(t)\rangle$ is the many-electron wave function, represented by a time-dependent single Slater determinant; $c_m^\dagger(c_n)$ are creation (annihilation) operators; and n and m refer to atomic orbital (AO) basis functions. For simplicity, we will assume the AO basis functions are orthonormal and linearly independent (e.g., in the semiempirical NDDO approximation, the vanishing overlap matrix is enforced by construction) and omit spin indices focusing on the description of pertinent singlet states. The formalism described in this work is also applicable to both ab initio TDHF and conceptually similar TDDFT methodologies, although the underlying details are more involved. To this end, we introduce a family of the single-electron density matrices defined as

$$(\rho_{\alpha\beta})_{mn} = \langle \phi_\alpha|c_m^\dagger c_n|\phi_\beta\rangle \tag{2}$$

where indices α and β label the adiabatic electronic eigenstates of the system (solutions of the time-independent electronic Schrodinger equation). From now on, we will omit matrix indices m and n and, unless otherwise specified, assume that all matrices are of $K \times K$ size, K being the basis set size. Thus, ρ_{00} is the ground-state density matrix,[69] whereas $\rho_{0\alpha} \equiv \xi_\alpha$ are transition density matrices (or electronic normal modes),[64] which represent changes in the density matrix induced by an optical transition from the ground state $|0\rangle$ to some excited state $|\alpha\rangle$. Within the TDHF approximation, these quantities are the eigenfunctions of the two-particle Liouville operator L from the linearized TDHF equation of motion[64,68]

$$L\xi_\alpha = \Omega_\alpha \xi_\alpha \tag{3}$$

In this equation, the eigenvalues Ω_α represent the electronic transition energies of the $|0\rangle \rightarrow |\alpha\rangle$ excitation. The eigenvectors obey the following normalization conditions

$$\langle \xi_\alpha|\xi_\beta\rangle = \mathrm{Tr}(\rho_{00}[\xi_\alpha^\dagger \xi_\beta]) = \delta_{\alpha,\beta} \tag{4}$$

where trace includes both spatial and spin variables. Equation 3 can be recast in the molecular orbital (MO) representation in a matrix form[64,68]

$$\begin{pmatrix} A & B \\ -B & -A \end{pmatrix}\begin{bmatrix} X \\ Y \end{bmatrix} = \Omega \begin{bmatrix} X \\ Y \end{bmatrix} \tag{5}$$

known as the first-order random phase approximation (RPA) eigenvalue equation where X and Y are particle−hole and hole−particle components of the transition density matrix

$$\xi = \begin{bmatrix} X \\ Y \end{bmatrix}$$

in the MO representation, respectively. An approximate solution to the full matrix equation can be found by neglecting B, resulting in a simplified eigenvalue equation

$$AX = \Omega X \tag{6}$$

where the matrix A is identical to the CIS matrix. This is also known as the Tamm−Dancoff approximation. The CIS approximation reduces the non-Hermitian matrix L to the Hermitian matrix A allowing for faster diagonalization. The Hermitian matrix B represents the higher-order electronic correlations included in the TDHF approximation and is known as the de-excitation operator.

As all modern RPA codes, the CEO procedure utilizes a very efficient Davidson diagonalization technique[70−73] at the CIS or TDHF level for computing the excitation frequencies at $\mathcal{O}(N^3)$ numerical cost, thus avoiding the computational bottleneck of the direct diagonalization of the Liouville operator ($\mathcal{O}(N^6)$ cost). This is possible since the action of the operator L on an arbitrary single electron matrix ξ can be calculated on the fly without constructing and storing the full matrix L in memory (direct approach)[64,71,74]

$$L\xi = [F(\rho_{00}), \xi] + [V(\xi), \rho_{00}] \tag{7}$$

where $F(\rho_{00})$ is the Fock matrix with matrix elements

$$F_{mn}(\rho_{00}) = t_{mn} + V_{mn}(\rho_{00}) \tag{8}$$

and an action of the Coulomb-exchange electronic operator V on an arbitrary matrix ξ is given by

$$V_{mn}(\xi) = \sum_{kl}^{K} \xi_{kl}\left((mn|kl) - \frac{1}{2}(mk|nl)\right) \tag{9}$$

In eqs 8 and 9, indices m, n, k, and l run over the basis functions; t_{nm} is the single-electron Hamiltonian describing the kinetic energy and nuclear attraction of an electron; and $(mn|kl)$ are conventional two-electron integrals representing electron−electron Coulomb interactions. The semiempirical approximation truncates the basis set to the valence functions and retains only a few essential two-electron integrals. Consequently, it is possible to avoid numerically demanding direct Fockian formation in ab initio techniques and treat very large molecular systems.

A unified description of correlated many-electron systems has been established based on the CEO representation of optical response: Namely, a many-electron system is mapped onto a set of coupled oscillators (quasi-particles), and optical nonlinearities are interpreted in terms of quasi-particle scattering.[64,65]

The TDHF approximation accounts for essential electronic correlations (electron−hole interactions plus some additional higher-order terms),[68,75] which is sufficient for a reasonably accurate calculation of UV−visible spectra in many extended organic molecular systems.[64] It has the advantage of being size consistent,[76] a major failure of truncated CI techniques.[77] However, excited states with a significant double excitation character (e.g., A_g states in polyacetylene) cannot be represented accurately with the TDHF and CIS methods.[78] Nevertheless, the CEO has been successfully applied to many molecular systems, including analysis of absorption spectra of conjugated polymers,[65,79−81] size-scaling of polarizabilities in donor/acceptor substituted conjugated molecules,[82−84] localized optical excitations in dendrimers,[85−87] and study of electronic excitations in various conjugated and biological aggregates and complexes.[88,89] Several extensions of the CEO concepts to TDDFT have also been made.[90−92]

B. Analytic Gradients and Nonadiabatic Couplings. Within the Born−Oppenheimer Approximation, the PES of ground and excited states of a molecule are well-defined, and their energies and many-body wave functions depend parametrically on the set of nuclear coordinates $\mathbf{R}$ (e.g., $E_0(\mathbf{R})/\phi_0(\mathbf{R})$ and $E_\alpha(\mathbf{R})/\phi_\alpha(\mathbf{R})$, $\alpha > 0$, being energies/wavefucntions of the ground and excited states, respectively) (see Figure 1, bottom panel). To propagate the MD trajectory along the PES or optimize molecular geometry, the respective gradients (forces) $\nabla E_\alpha(\mathbf{R}) \equiv (\partial E_\alpha)/(\partial \mathbf{R})$ should be calculated efficiently. This is achieved by analytic gradient techniques (as opposed to the much slower numerical differentiation) expressing the energy gradients in terms of derivatives of the Hamiltonian matrix elements. The situation is simple for ground-state energy obtained with the variational self-consistent field (SCF) procedure where, according to the variational principle, the gradients of the ground-state energy become

$$\frac{\partial E_0}{\partial \mathbf{R}} = \frac{1}{2}\mathrm{Tr}((t^{(R)} + F^{(R)})\rho_{00}) \tag{10}$$

where trace includes both spatial and spin variables. The derivatives of $t^{(R)}$ and $F^{(R)} = t^{(R)} + V^{(R)}(\rho_{00})$ with respect to the nuclear degrees of freedom apply only to the matrix elements of one-electron and two-electron operators (eq 8), which are routinely calculated in all quantum-chemical packages.

Computation of derivatives of the excited-state energies $E_\alpha = E_0 + \Omega_\alpha$ is more involved (note that the derivative of Ω_α obtained directly via expression $\Omega_\alpha = \langle\xi_\alpha|L\xi_\alpha\rangle$ is nonvariational with respect to the transition density ξ_α). An elegant variational formulation of the TDDFT (and TDHF) techniques introduced in refs 93 and 94 allows this deficiency to be overcome. In this method, the excited states are obtained variationally from the specific functional required to be stationary with respect to all parameters. We refer the reader to a detailed derivation in refs 93−95 and here give the final result for the gradients of the transition energy Ω_α

$$\frac{\partial \Omega_\alpha}{\partial \mathbf{R}} = \mathrm{Tr}(F^{(R)}p_{\alpha\alpha}) + \mathrm{Tr}(V^{(R)}(\xi_\alpha^\dagger)\xi_\alpha) \tag{11}$$

where $p_{\alpha\alpha}$ is related to the excited-state density matrix (see eq 2) $\rho_{\alpha\alpha} = \rho_{00} + p_{\alpha\alpha}$, and, in turn, is composed of two terms

$$p_{\alpha\alpha} = [[\xi_\alpha^\dagger, \rho_{00}], \xi_\alpha] + Z_{\alpha\alpha} \tag{12}$$

where the square brackets denote an anticommutator of two matrices.

$$T_{\alpha\alpha} = [[\xi_\alpha^\dagger, \rho_{00}], \xi_\alpha] \equiv (I - 2\rho_{00})(\xi_\alpha^\dagger\xi_\alpha + \xi_\alpha\xi_\alpha^\dagger) \tag{13}$$

is the so-called unrelaxed part of the excited-state density matrix, where I is the unit matrix. Finally, the $Z_{\alpha\alpha}$ matrix, accounting for orbital relaxation effects, can be found by solving a linear equation

$$LZ_{\alpha\alpha} = -\left[\left([[\rho_{00}, \xi_\alpha^\dagger], V(\xi_\alpha)] + V\left(\frac{1}{2}[[\xi_\alpha^\dagger, \rho_{00}], \xi_\alpha]\right)\right), \rho_{00}\right] \tag{14}$$

Mapping a TDHF/TDDFT equation of motion into the dynamics of a coupled system of electronic oscillators allows expressions for nonlinear optical response of the systems to be derived,[64,81,95] which, in particular, leads to an alternative form of $Z_{\alpha\alpha}$ via an expansion into the transition density matrices

$$Z_{\alpha\alpha} = -\sum_\beta \frac{V_{-\alpha\alpha\beta}}{\Omega_\beta}\xi_\beta,\ \beta = -M, \ldots, M \tag{15}$$

where $V_{-\alpha\alpha\beta}$ is a three-point Coulomb matrix element given by eq 21.[64,81,95] This summation includes negative indices defined using the convention $\Omega_{-\beta} = -\Omega_\beta$ and $\xi_{-\beta} = \xi_\beta^\dagger$ and runs up to the number of all excited states in the TDHF approximation $M = N_p \times N_h$ (N_p (N_h) being the number of occupied (virtual) orbitals). Consequently, for practical purposes it is more convenient and accurate to use eq 14 for calculating $Z_{\alpha\alpha}$ and to obtain excited-state analytical gradients as $(\partial E_\alpha/\partial \mathbf{R}) = (\partial E_0/\partial \mathbf{R}) + (\partial \Omega_\alpha/\partial \mathbf{R})$. We note that the contribution of $Z_{\alpha\alpha}$ into $\rho_{\alpha\alpha}$ is significant (being ∼10−40%) compared to the contribution of $T_{\alpha\alpha}$ in several molecular examples we considered, which is consistent with the previous studies.[93]

The final ingredient from the electronic structure calculations necessary for MDQT methodology outlined below is the nonadiabatic coupling between excited states defined as

$$\mathbf{d}_{\alpha\beta} = \langle\phi_\alpha(R)|\nabla_R\phi_\beta(R)\rangle, \alpha \neq \beta \tag{16}$$

These quantities (further denoted as NACR) can also be calculated analytically following methodology developed by Chernyak and Mukamel making use of the Hellmann−Feynman theorem[96,97]

$$\mathbf{d}_{\alpha\beta} = \frac{\mathrm{Tr}(F^{(R)}\rho_{\alpha\beta})}{\Omega_\alpha - \Omega_\beta}, \alpha \neq \beta \tag{17}$$

equivalent to eq 4 in ref 97 and $\mathbf{d}_{\alpha\alpha} = 0$. Similarly, time-dependent NA coupling (NACT) derived from eq 17 is given by

$$\dot{\mathbf{R}}\cdot\mathbf{d}_{\alpha\beta} = \left\langle\phi_\alpha\middle|\frac{\partial\phi_\beta}{\partial t}\right\rangle = \frac{\mathrm{Tr}(F^{(t)}\rho_{\alpha\beta})}{\Omega_\alpha - \Omega_\beta} \tag{18}$$

where $\dot{\mathbf{R}} = (\partial\mathbf{R}/\partial t)$ are nuclear velocities, and $F^{(R)}$ and $F^{(t)}$ denote the respective derivatives of the matrix elements of the Fock operator (eq 8).

As in the case of the excited-state gradients, the key quantity here is the transition density matrix between excited states $\rho_{\alpha\beta}$, calculation of which involves both relaxed and unrelaxed parts (compare to eq 12).

$$\rho_{\alpha\beta} = [[\xi_\alpha^\dagger, \rho_{00}], \xi_\beta] + Z_{\alpha\beta} \tag{19}$$

The variational formalism to calculate the unrelaxed part $Z_{\alpha\beta}$ is yet to be developed. Instead, we use an expansion of $Z_{\alpha\beta}$ into ground-to-excited-state transition density matrices derived from the nonlinear optical response formalism,[64,81,95] which is analogous to eq 12

$$Z_{\alpha\beta} = \sum_{\gamma} \frac{V_{-\alpha\beta\gamma}}{-\Omega_{\alpha}+\Omega_{\beta}-\Omega_{\gamma}} \xi_{\gamma},\ \gamma = -M, \ldots, M \quad (20)$$

where the Coulomb matrix element $V_{\alpha\beta\gamma}$ is given by

$$V_{\alpha\beta\gamma} = \frac{1}{2}\sum_{\alpha\beta\gamma}^{\text{perm}} \mathrm{Tr}((I-2\rho_{00})\xi_{\alpha}\xi_{\beta}V(\xi_{\gamma})) \quad (21)$$

Here, the $V_{\alpha\beta\gamma}$ tensor is symmetrized with respect to all permutations of its indices α, β, and γ. We note that contribution of $Z_{\alpha\beta}$ into $\rho_{\alpha\beta}$ is small (being $\sim$5−10%) compared to the contribution of $T_{\alpha\beta}$ in all molecular examples we considered. Due to a larger energy gap, the contribution to expansion (eq 20) from excited states ϕ_{γ} with the higher energy than ϕ_{α} and ϕ_{β} states is very small. Consequently, we truncate the summation (eq 20) up to the number of excited states $\mathscr{M}_{\text{eff}}$ included in the NA simulation.

C. Molecular Dynamics Simulations and Surface Hopping Method. The evolution of the molecules after initial photoexcitation is followed using the ESMD approach[29] to calculate classical nuclear trajectories on the excited-state adiabatic PES. The ESMD approach proved to be an adequate theoretical tool to model various photophysical dynamical processes (e.g., coherent phonon dynamics, exciton−phonon coupling, exciton self-trapping, breathers) in many organic materials such as conjugated polymers and carbon nanotubes[29,34,35,98−100] as well as simulation of nonadiabatic dynamics leading to energy transfer in conjugated dendrites.[59,60] A schematic representation of the computations is shown in Figure 1, bottom panel: a molecule, initially in a given ground-state geometry, is photoexcited creating an exciton. After the initial photoexcitation, evolution of the nuclear degrees of freedom continues along the excited-state potential energy surface $E_{\alpha}(\mathbf{R})$ according to the Langevin equation of motion[101]

$$M_i\ddot{\mathbf{R}}_i(t) = -\nabla E_{\alpha}(\mathbf{R}(t)) - \zeta M_i\dot{\mathbf{R}}_i(t) + \mathbf{A}(t) \quad (22)$$

Here M_i, $\ddot{\mathbf{R}}_i$, $\dot{\mathbf{R}}_i$, and $\mathbf{R}_i$ represent the mass, acceleration, velocity, and position of the ith nuclei, respectively. Cartesian coordinates ($\mathbf{R}_i = X_i, Y_i, Z_i$) are used as propagation coordinates. The stochastic force $\mathbf{A}$ depends on the bath temperature T and the friction coefficient ζ (ps^{-1}). It obeys the fluctuation−dissipation theorem satisfying the condition:[101] $\langle \mathbf{A}_i(t)\cdot\mathbf{A}_j(t+\Delta t)\rangle = 2M_i\zeta k_{\mathrm{B}}T\delta(\Delta t)\delta_{ij}$, where the symbol $\langle\ldots\rangle$ denotes an equilibrium average over time; k_{B} is the Boltzmann constant; and $\delta(\Delta t)$ and δ_{ij} are the Dirac and Kronecker delta functions, respectively. A numerical velocity Verlet[58,102] finite difference algorithm is used to integrate the equations of motion. We implement a constant-temperature Langevin dynamics algorithm, developed to be consistent with the velocity Verlet integration technique,[103] and utilize a random number generator following numerical recipes.[104] The excited-state PES $E_{\alpha}(\mathbf{R})$ in eq 22 is calculated quantum mechanically using the CEO method as $E_{\alpha}(\mathbf{R}) = E_0(\mathbf{R}) + \Omega_{\alpha}(\mathbf{R})$, and the analytical gradient technique, outlined in the previous section, is used to efficiently propagate the trajectory along the α PES.

To account for quantum transitions among the adiabatic excited-state PES, we employ molecular dynamics with quantum transitions (MDQT) where the probabilities of quantum transitions are determined by the fewest switches surface hopping (FSSH) algorithm of Tully.[46] A swarm of N classical trajectories (wavepacket) is propagated. At any point in time, the nuclei of each trajectory are evolved on a single adiabatic potential energy surface rather than in the mean field. The nuclei are treated classically while the electrons are treated within the quantum mechanical framework, and the system is allowed to transition (or hop) between electronic states depending on the strength of the nonadiabatic (NA) coupling.[46,47] The MDQT approach allows quantum transitions at any time between any number of coupled states. Within an independent trajectory approximation, the observables (such as decay rates) are statistical averages over all trajectories propagated. The FSSH switching procedure ensures that, for a large ensemble of trajectories, the fraction of trajectories assigned to any state at any time is equal to the average quantum probability at that time. Such simulations increase an associated numerical expense by 2−3 orders of magnitude compared to a single trajectory MD.[29,34] Subsequently, the efficiency of the ESMD method plays a critical role in allowing the classical nuclear trajectories to be propagated on the actual excited-state adiabatic potential energy surfaces.

For every single trajectory, the forces on the classical subsystem are determined by a single adiabatic eigenstate, the occupied state α in eq 22, whereas the total electronic wave function is a mixed state, expanded in terms of the adiabatic basis functions

$$\Psi(x,R,t) = \sum_{\alpha} c_{\alpha}(t)\phi_{\alpha}(r;\mathbf{R}(t)) \quad (23)$$

where $c_{\alpha}(t)$ are the time-dependent expansion coefficients, and $\mathbf{R}$ are the electronic degrees of freedom. The equation of motion for the coefficients $c_{\alpha}(t)$ can be generated by substituting eq 23 into the time-dependent Schrodinger equation. The resulting expression simplifies in the adiabatic Hamiltonian eigenstates $\{\phi_{\alpha}\}$ yielding

$$i\hbar\frac{\partial c_{\alpha}(t)}{\partial t} = c_{\alpha}(t)E_{\alpha} - i\hbar\sum_{\beta} c_{\beta}(t)\,\dot{\mathbf{R}}\cdot\mathbf{d}_{\alpha\beta} \quad (24)$$

where the NACR vector $\mathbf{d}_{\alpha\beta}$ and the NACT scalar $\dot{\mathbf{R}}\cdot\mathbf{d}_{\alpha\beta}$ are given by eqs 16−18. The diagonal elements of the time-dependent density matrix with elements $a_{\alpha\beta}(t) = c_{\alpha}^{*}(t)c_{\beta}(t)$ give the occupation probabilities of the instantaneous adiabatic eigenstates.

The FSSH algorithm allows systems to hop to another adiabatic state at any point in time t, and the probability that the nuclear trajectory will hop from the current electronic state α to some other state β during the time interval Δt is

$$g_{\alpha\beta} = \Delta t\,\frac{b_{\beta\alpha}(t)}{a_{\alpha\alpha}(t)} \quad (25)$$

where $a_{\alpha\alpha}(t) = c_{\alpha}^{*}(t)c_{\alpha}(t)$ and $b_{\beta\alpha}(t) = -2Re(a_{\alpha\beta}^{*}\dot{\mathbf{R}}\cdot\mathbf{d}_{\alpha\beta})$. The quantity $b_{\beta\alpha}$ is related to the probability flux $\dot{a}_{\alpha\alpha}(t) = \Sigma_{\alpha\neq\beta}b_{\alpha\beta}(t)$. Note that $g_{\alpha\beta} = -g_{\beta\alpha}$ and $g_{\alpha\alpha} = 0$, since $\mathbf{d}_{\alpha\beta} = -\mathbf{d}_{\beta\alpha}$ and $\mathbf{d}_{\alpha\alpha} = 0$ (see Section IIB). At each integration time step Δt, the switching probability $g_{\alpha\beta}$ is calculated, and a uniform random number $0 < \varsigma < 1$ is generated (following numerical recipes[104]) to determine whether or not the transition will occur. If the calculated $g_{\alpha\beta}$ is negative (unphysical value), then the switching

probability is set to zero, thereby minimizing the number of hops. Let us assume that the states are ordered with an increase of their transition energy. The hop from the state α to another state β is performed if

$$\sum_{\gamma=1}^{\beta} g_{\alpha\gamma} < \varsigma \leq \sum_{\gamma=1}^{\beta+1} g_{\alpha\gamma} \tag{26}$$

Finally, if $\sum_{\gamma=1}^{\mathscr{M}_{\text{eff}}} g_{\alpha\gamma} < \varsigma < 1$ then the system remains in state α, $\mathscr{M}_{\text{eff}}$ being the total number of states included in the simulation (typically $\mathscr{M}_{\text{eff}} \ll \mathscr{M}$).

After the hop, the nuclear trajectory will begin to evolve on the PES of the new state, and the nuclear velocities are rescaled along the direction of the electronic component of the NA coupling[105] to conserve the total electron−nuclear energy. If a hop to an electronic state of higher energy is predicted and the kinetic energy available in the nuclear coordinates along the direction of the NA coupling is insufficient, then the hop is rejected. The velocity adjustment procedure has been discussed elsewhere in detail.[50] Ultimately, velocity rescaling and hop rejection creates a detailed balance between transitions to higher and lower energy.[106]

D. Consistent Propagation of Nuclear and Electronic Degrees of Freedom. To solve eq 24 numerically, we separate the time evolution into real and imaginary parts of $c_\alpha(t)$ by expressing the coefficients as $c_\alpha = \sigma_k e^{i\theta\alpha}$, which leads to the coupled equations

$$\dot{\sigma_\alpha} = -\sum_{\beta} \sigma_\beta \cos(\theta_\beta - \theta_\alpha)\dot{\mathbf{R}}\cdot\mathbf{d}_{\alpha\beta} \tag{27}$$

$$-\hbar\sigma_\alpha\dot{\theta_\alpha} = \sigma_\alpha E_\alpha + \hbar\sum_{\beta} \sigma_\beta \sin(\theta_\beta - \theta_\alpha)\dot{\mathbf{R}}\cdot\mathbf{d}_{\alpha\beta} \tag{28}$$

The Runge−Kutta−Verner fifth- and sixth-order method based on a code designed by Hull, Enright, and Jackson[107,108] is then used to solve the initial-value problem for the ordinary differential eqs 27 and 28.

Thus, eqs 22, 27, and 28, solved simultaneously along the trajectory $\mathbf{R}(t)$, constitute the essence of the hybrid quantum/classical propagation. Excited-state energies $E_\alpha(\mathbf{R})$ and analytic gradients $\nabla E_\alpha(\mathbf{R})$ entering eq 22 are calculated on the fly during the molecular dynamics simulations at every trajectory point $\mathbf{R}(t)$ with the time step Δt being used for the propagation of the nuclei with the Velocity Verlet algorithm. Nevertheless, the variations in time of the real and imaginary parts of the quantum coefficients (eqs 27 and 28) require a smaller quantum time step $\delta t \leq \Delta t$. Therefore, the excited-state energies $E_\alpha(\mathbf{R})$ and all of the $N(N-1)/2$ NACT couplings $\dot{\mathbf{R}}\cdot\mathbf{d}_{kj}$ are evaluated at each classical time step and at each intermediate value with δt time interval, so that no approximations[109] have been made in this respect. The values of the nuclear coordinates at $t + n\delta t$ ($n = 0, \ldots, N_q - 1 = (\Delta t/\delta t) - 1$) are obtained using the Velocity Verlet equations with values of $\ddot{\mathbf{R}}_i$ and $\dot{\mathbf{R}}_i$ evaluated at t. Furthermore, the Runge−Kutta−Verner fifth- and sixth-order method, used to integrate eqs 27 and 28, also requires the values of energies and NACT couplings at many points in the interval $[t + n\delta t,\ t + (n+1)\delta t]$. We use a simple linear interpolation and extrapolation scheme to obtain those values, where the number of steps used for interpolation is variable and depends on how fast the quantum mechanical quantities change with time.

The use of two different methods applied for classical and quantum propagations can be justified according to the advantages and disadvantages of each of them.[58] The Runge−Kutta-like methods are more accurate but computationally more expensive than the Verlet methods. This is particularly the case at small integration time steps. Nevertheless, the Verlet-like methods allow for larger integration time steps with a reasonable accuracy. The calculations of NACT couplings are independent of the calculation of excited-state gradients, so that the computational cost is reduced for longer classical time steps.

It is important to stress that the switching probabilities $g_{\alpha\beta}$ (eq 25) are evaluated at each classical step Δt. Nevertheless, this time interval is typically too large to guarantee the applicability of eq 25. Therefore, according to Tully and Hammes-Schiffer,[105] the following equation has been applied

$$g_{\alpha\beta} = \frac{\sum_{j=1}^{N_q} b_{\beta\alpha}(j)\delta t}{a_{\alpha\alpha}} \tag{29}$$

where $N_q = (\Delta t/\delta t)$ is the number of quantum steps per classical integration step.

E. NA-ESMD Implementation . *Preparation of the Wavepacket.* A swarm of classical trajectories are propagated in the MDQT approach. Preparation of the initial conditions (snapshots of the molecular geometry $\mathbf{R}$ with the respective set of nuclear velocities $\dot{\mathbf{R}}$) is a critical preliminary step in the simulations. The initial sampling of conformational space (before any electronic excitation takes place) should be adequate to represent the equilibrated ensemble of molecules at given thermodynamic conditions. Typically, this requires computing a long BO ground-state trajectory of the system using eq 22 with parameters (temperature T and friction coefficient ζ) consistent with the future excited-state simulations. Depending on the molecular system, the snapshots can be taken every ∼1−10 ps after the molecule has been equilibrated in the ground state for ∼10−50 ps. This allows initialization of nuclear coordinates $\mathbf{R}$ and velocities $\dot{\mathbf{R}}$ from these snapshots to form a wavepacket for the excited-state MDQT simulations. The next step is to populate initial excited states (i.e., set the initial values of the quantum coefficients) according to a laser excitation wavelength, a laser pulse width, excited-state transition dipole moments/oscillator strengths, etc. The total number of propagated excited states $\mathscr{M}_{\text{eff}}$ should be sufficiently large to include possible upward hops to the higher-energy states.

MDQT Modeling. After assigning the initial conditions, the NA-ESMD algorithm calculates every trajectory as follows:

(1) Propagate nuclei in the interval $t \rightarrow t + \Delta t$ along the α excited-state PES following eq 22. The ESMD gradients $\nabla E_\alpha(\mathbf{R})$ (eqs 10 and 11) are evaluated at t.
(2) Propagate the absolute values and phases of the quantum coefficients in the N_q intervals $[t + n\delta t,\ t + (n+1)\delta t]$ ($n = 0, \ldots, N_q - 1$). At each interval, the excited-state energies $E_\alpha(\mathbf{R})$ and NACT couplings $\dot{\mathbf{R}}\cdot\mathbf{d}_{\alpha\beta}(t)$ (eq 18) are calculated using nuclear coordinates evaluated at $t + n\delta t$ with velocities and gradients computed at t.
(3) Evaluate the switching probabilities $g_{\alpha\beta}$ (eq 29) using the NACR $\mathbf{d}_{\alpha\beta}$ values computed with eq 17. Generate a random number[104] and determine whether a switch to another potential energy surface occurs using eq 26. If a hop $\alpha \rightarrow \beta$ is realized, velocities are adjusted, and the nuclei will continue to propagate on the β state PES (i.e., $\alpha = \beta$).
(4) Store relevant data and return to step (2).

Note 1. In our previous work,[59,60] we used an alternative procedure for evaluation of NACT couplings $\dot{\mathbf{R}}\cdot\mathbf{d}_{kj}$ at each of the N_q quantum time steps performed per classical step, which is a linear interpolation of these quantities between classical points following.[50,105] This approach, however, severely limits the size of the classical integration step (typically less than $\Delta t = 0.05$ fs with $N_q \sim 10$ quantum steps in between) to ensure the validity of the interpolated values. Our new algorithm, described in Section IID, requires direct evaluation of the excited-state energies $E_\alpha(\mathbf{R})$ and NACT couplings $\dot{\mathbf{R}}\cdot\mathbf{d}_{\alpha\beta}$ at each of the N_q quantum time steps performed per classical step. This, in principle, seems to be computationally expensive. However, this approach lifts the previous limitations since interpolations take place only at intermediate times within quantum time steps according to requirements of the Runge−Kutta−Verner method. Therefore, the computational cost increased by the calculation of $E_\alpha(\mathbf{R})$ and $\dot{\mathbf{R}}\cdot\mathbf{d}_{kj}$ at each quantum step can be compensated by the enlargement of the classical step and smaller number of quantum steps N_q per classical step that can be chosen without losing precision in the quantum propagation. We have observed that typical values of 3−5 quantum steps per classical steps of 0.1−0.2 fs provide sufficient accuracy for several molecular systems, which reduces computational time by 2−3 times compared to the old code.

Note 2. The NA-ESMD computational efficiency critically depends on the quality of the initial guess for the ground-state density matrix ρ_{00} (SCF procedure) and initial guesses of the transition densities ξ_α, $\alpha = 1, ..., \mathscr{M}_{\text{eff}}$ (Davidson's iterations). Consequently, reuse of these data from the previous trajectory point improves computational efficiency by nearly an order of magnitude. It is worth mentioning that the overall sign of the transition density matrices ξ_α may infrequently change for two subsequent points of the trajectory due to various numerical reasons in Davidson's algorithm (i.e., $\xi_\alpha(t) \sim -\xi_\alpha(t+\delta t)$, here both $\xi_\alpha(t)$ and $\xi_\alpha(t+\delta t)$ are valid calculated eigenvectors in eq 3). In this case, incorrect NACT couplings may be obtained according to eqs 16−18. To avoid these spontaneous changes of sign, the relative phase of these quantities should be tracked at each integration step; i.e., if $\langle\xi_\alpha(t)|\xi_\alpha(t+\delta t)\rangle < 0$ (see eq 4), then $\xi_\alpha(t+\delta t) \rightarrow -\xi_\alpha(t+\delta t)$.

III. NA-ESMD MODELING OF PHOTOINDUCED DYNAMICS IN DISTYRYLBENZENE

A. Molecular Dynamics Simulations. The top panel in Figure 4 shows the chemical structure of *trans*-distyrylbenzene which is a small oligomer of polyphenylene vinylene. For all simulations presented here, we use the AM1/CIS level of theory. We start with analysis of the excited-state structure calculated at the ground-state optimal geometry. The top panel in Figure 4 shows the computed density of singlet excited states with transition energies in a 0−8 eV spectral window. Due to inversion symmetry (barring the conformational disorder), all states have either A_g- or B_u-like symmetry, which is a typical case for all conjugated polymers. For example, the ground state S_0 has A_g symmetry. The middle panel in Figure 2 displays the normalized linear absorption spectrum of distyrylbenzene calculated for the ground-state optimized structure from the transition energies Ω_α and their respective oscillator strengths f_α utilizing Gaussian line broadening

$$\chi(\omega) = \sum_\alpha f_\alpha \exp\frac{-(\Omega_\alpha-\omega)^2}{\Gamma^2} \qquad (30)$$

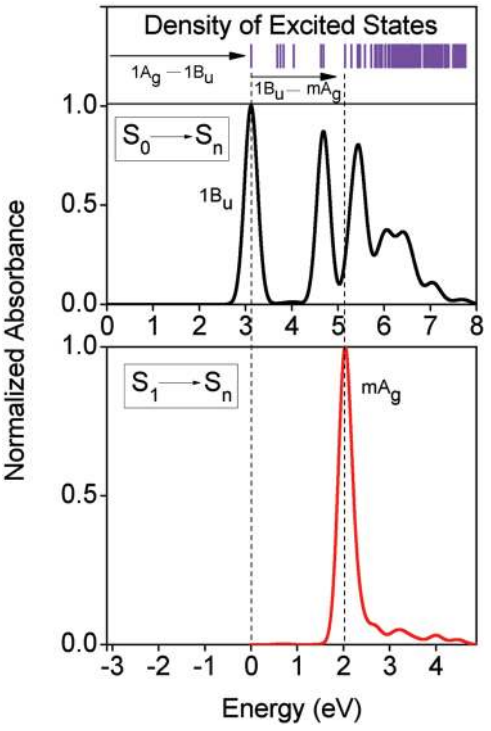

Figure 2. Top: calculated density of excited states. Middle: calculated ground $1A_g$ (S_0) state absorption spectrum. Bottom: calculated excited $1B_u$ (S_1) absorption spectrum. The mA_g (S_m) state is optically accessible from S_1 but not from the ground state. The spectral lineshapes are calculated using eq 30 with empirical line width $\Gamma = 0.1$ eV.

The lowest excited-state S_1 has B_u symmetry, and consequently the transition $1A_g \rightarrow 1B_u$ is optically allowed appearing as a strong peak at 3.12 eV in the calculated absorption spectrum. The S_1 state is a primary band gap excitonic state in the luminescent conjugated polymers (like PPV) harvesting most of the oscillator strength and responsible for photoluminesce. The peaks at higher energy are attributed to the absorbance of the phenyl and vinyl groups consistent with the previous studies.[64,65] The bottom panel in Figure 2 shows the calculated absorption from the lowest-energy excited state S_1. It reveals a single strong absorbance feature separated from the $1B_u$ state by 2.0 eV which is assigned as the mA_g state. The mA_g (or S_m) transition is a significant state corresponding to a delocalized excitonic transition in the conjugated polymers[110] typically studied by an ultrafast pump−probe spectroscopy technique[62] revealing a fascinating picture of photoinduced dynamics in these materials. The AM1/CIS calculated spectra for S_1 and S_0 absorbances are in good agreement with experiment. Experimentally determined absorption spectra for distyrylbenzene place the $1B_u$ state at 2.74 eV (calculated vertical transition energy is 3.1 eV), and the mA_g has a 1.72 eV separation from S_1 (calculated value is 2.0 eV).[110−112]

Our next step is modeling of the photoinduced dynamics of *trans*-distyrylbenzene at both room temperature (300 K) and low temperature (10 K) cases. We start with computing the ground-state molecular dynamics simulations of two 300 ps long BO trajectories (300 K and 10 K) with the time step $\Delta t = 0.5$ fs. The system was heated and allowed to equilibrate to a final temperature of 300 K (10 K) during the first 10 ps. The Langevin thermostat[103] (eq 22) was used to keep the temperature constant

with a friction coefficient $\zeta = 2.0\ \mathrm{ps}^{-1}$. Although high-temperature thermalization offers an effective route to generate conformational sampling,[113] in this case thermalization was performed at a room/low temperature to ensure that the fraction of *cis* conformers remained low. The rest of the trajectories was used to collect a set of initial positions and momenta for the subsequent simulations of the excited states. Configurations were sampled with intervals of 0.5 ps for a total of 540 configurations per ground-state trajectory. All of the subsequent data should be interpreted as the average value over the swarm of 540 trajectories.

Excited-state dynamics trajectories were started from these initial configurations after photoexcitation. The persistent large gap (~3 eV) between the ground and the first excited state excludes nonradiative relaxation to the ground state during picosecond dynamics and allows us to avoid the limitations in describing ground-state/first excited-state conical intersections imposed by methods based on the single reference ground-state description. We considered three distinct cases. Case I: Dynamics of the $1A_g$ (or S_0) ground state in which no photoexcitation was produced. Here the nuclei are propagated on a single BO PES. These simulations serve as a reference point. Case II: Dynamics after a vertical excitation to the lowest excited $1B_u$ (or S_1) state. Again, the nuclei are propagated on a single BO PES of the S_1 state. Finally, case III corresponds to the photoexcited dynamics after populating the highly excited mA_g (or S_m) state. Here we target photoinduced dynamics of the interband relaxation (see Figure 1) via multiple BO surfaces as the system passes nonadiabatic regions and state switches occur. Twenty lowest excited states have been calculated for every snapshot to determine the mA_g state by selecting a transition with the highest oscillator strength from the $1B_u$ state. We found that for the S_m state, $m = 9$ for all snapshots taken from the 10 K ground-state trajectories, whereas m varied from 8 to 12 for initial geometries taken at 300 K due to large conformational disorder induced by thermal fluctuations. We further use NA-ESMD code to propagate all trajectories for 1 ps at 300 K and 10 ps at 10 K. A classical step $\Delta t = 0.1$ fs and $N_q = 3$ quantum steps were used in all simulations, resulting in a few hours of computational time at most for the longest 10 ps nonadiabatic trajectories. Finally, $\mathscr{M}_{\mathrm{eff}} = 15$ excited states were included for simulation of S_m trajectories to allow upward energy transitions. Overall, we observe only a few hops to the higher excited-state energies.

B. Analysis of Electronic Dynamics. The top panels in Figure 3 show variation of the potential energies averaged over 540 trajectories during the S_0, S_1, and S_m simulations. As expected, the potential energy remains constant during simulation of the ground state evidencing that the simulated wavepaket represents well-equilibrated conformational space of the molecule. Traces of the thermal fluctuations at 300 K appear as small noise along the line. After the S_1 photoexcitation, the system is drawn far from the equilibrium, and a complex electron-vibrational dynamics occurs where the excess of vibrational energy is dissipated to phonons and, subsequently, damped into the bath (thermostat) degrees of freedom. This vibrational relaxation occurring on a single BO surface is manifested in the S_1 dynamics as an ultrafast drop (within ~100 fs) in the potential energy as the system decays close to the minimum of the potential energy well (see insets in Figure 3). A few wiggles in the beginning of the trajectories (0−30 fs) at both 300 K and 10 K correspond to a coherent (in phase) C=C vibrational excitation (see the next section) across the ensemble of all snapshots (i.e., coherent phonons). The potential energy varies with a period of ~9 fs, which is related

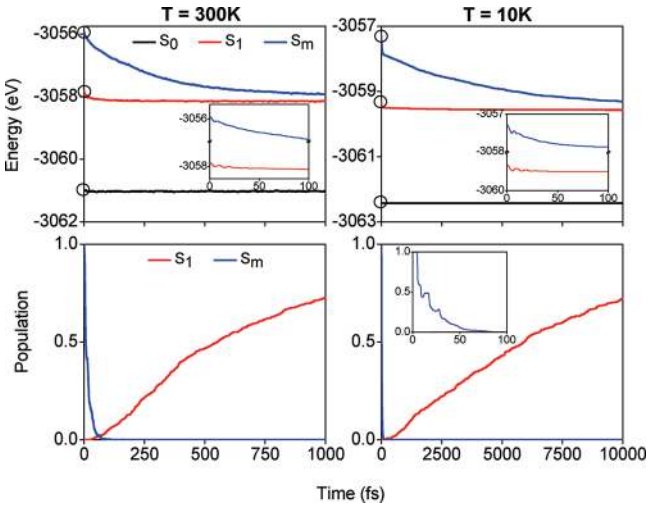

Figure 3. Top: Variation of averaged potential energy during dynamics at $T = 300$ K and $T = 10$ K. The insets show the ultrafast decrease in energy as S_1 and S_m undergo vibrational relaxation and dissipate energy to phonons. Bottom: Population of the mA_g and $1B_u$ states as a function of time obtained from the fraction of trajectories in each state at $T = 300$ K and $T = 10$ K. In both cases, decay of population from the mA_g state is complete within 50 fs. The low temperature severely delays the population transfer to the lowest-energy $1B_u$ excited state.

to a doubled frequency of the C=C stretching motion.[98] Following vibrational relaxation, S_1 remains at a constant average energy.

Both Born−Oppenheimer and nonadiabatic dynamics occur simultaneously in the S_m simulations. The molecule undergoes vibrational relaxation on a single PES and can also hop to a different electronic state where the system will undergo vibrational relaxation on the new PES. In the low-temperature case, the state switches are less frequent, and the nonadiabatic dynamics is "slow". Consequently, the potential energy during the first 100 fs at 10 K reflects BO vibrational relaxation of S_m to be significantly larger compared to that of S_1 (see insets in Figure 3). For the room-temperature case, the nonadiabatic dynamics is fast, and it is impossible to distinguish between BO vibrational relaxation and state hopping processes.

The average population of the initial mA_g state and the final $1B_u$ state during the S_m dynamics is plotted in the bottom panels in Figure 3. The ground state remains unpopulated throughout the course of the S_m simulation since the nonradiative relaxation over the large gap from excited states to the ground state occurs on a nanosecond time scale. At room temperature, the population of the initial mA_g state rapidly decays to zero within tens of femtoseconds. Fitting the data to the sum of two exponentials gives a fast component with a time constant of 8.3 fs and a slower component with a time constant of 18 fs. At low temperature, the decay of the initial S_m state is equally fast with time constants of 6.7 and 18 fs for the fast and slow component, respectively. Note that these ultrafast decay rates do not represent a depletion of the S_m population, which is particularly clear for the low-temperature dynamics. Instead, we have a case of a trivial state intersection when the system remains on the S_m diabatic states by going energetically below some other excited state (i.e., $m \rightarrow m - 1$) due to BO vibrational relaxation. During the course of the 1 ps dynamics, about 70% of the initial S_m population is transferred to the lowest-energy excited state at 300 K. However, at 10 K the rise of the lowest-energy excited-state population is severely retarded with less than 75% population transfer after 10 ps.

dx.doi.org/10.1021/jp109522g |J. Phys. Chem. B 2011, 115, 5402–5414

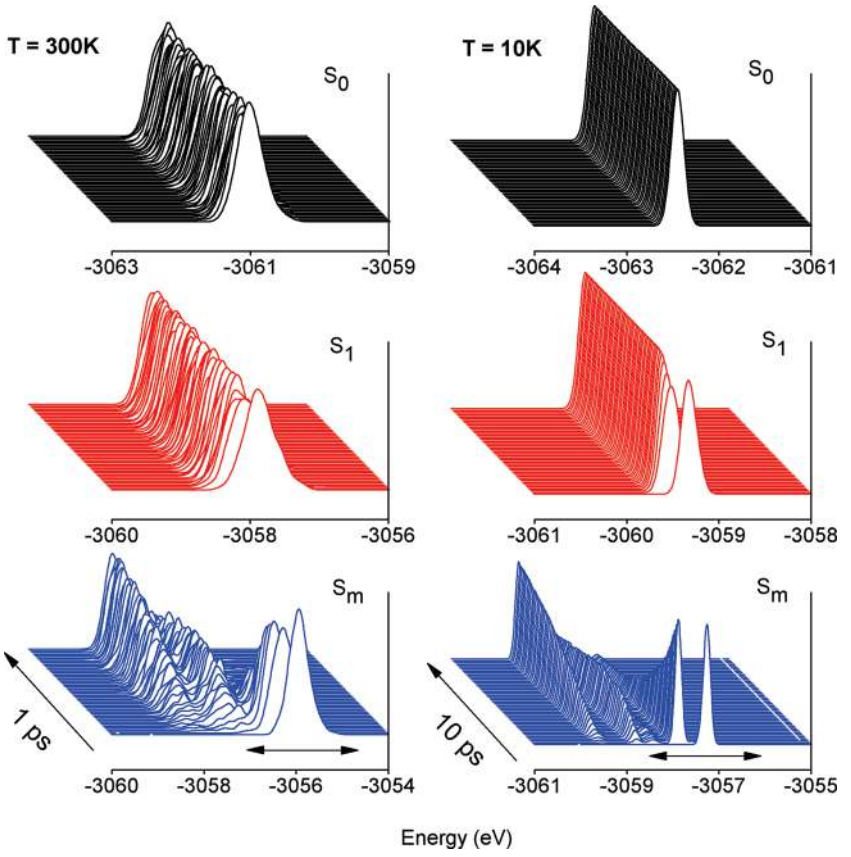

Figure 4. Wavepacket dynamics is constructed from energy histograms plotted at 20 and 200 fs intervals for T = 300 K and T = 10 K dynamics, respectively. The evolution of S_0 (top panel, black line), S_1 (middle panel, red line), and S_m (bottom panel, blue lines) wavepackets is shown. The S_m wavepacket branches into three distinct peaks due to large gaps in the density of the excited states.

We monitor a steady rise of S_1 population by fitting the curve to the function

$$f(t) = \frac{A\exp(t/\tau)}{A+\exp(t/\tau)} - \frac{A}{1+A} \qquad (31)$$

where t is time; τ is the relaxation time scale (inverse rate); and A is a normalization constant to ensure an appropriate population between 0 and 1. The population of the lowest-energy excited state is rising with a time constant of 394 fs. This can be directly compared with the time constant of 200 fs for $mA_g \rightarrow 1B_u$ relaxation in the PPV thin film obtained by ultrafast spectroscopic measurements.[62] Such slower relaxation in distyrylbenzene is expected. Compared to the polymer, the distyrylbenzene density of excited states (top panel in Figure 2) is low and has two large gaps. Additionally the $1B_u - mA_g$ energy gap in distyrylbenzene (1.74 eV) is much larger than that in PPV (0.8 eV). All these factors should slow down relaxation processes in distyrylbenzene compared to PPV. Our fitted time scale for the rise of S_1 population at 10 K is 4.2 ps.

Figure 4 shows the time evolution of the wavepackets corresponding to a swarm of propagated trajectories. Here the height of each point of the wavepacket corresponds to a fraction of trajectories (out of 540) having a given energy. As expected, at low temperature the ground-state wavepacket is very narrow and does not change in the course of the dynamics. At room temperature the wavepacket is much broader reflecting larger conformational space sampled due to thermal fluctuations. The S_1 wavepacket evolution is mostly similar to its ground-state counterpart, except that the vibrational relaxation toward the minimum of the S_1 PES pronounced in the beginning of the dynamics appears as the red shifts of the maxima at both 10 K and 300 K. The dynamics of the S_m wavepacket has several interesting features. First of all, large vibrational relaxation of the S_m state is clearly seen in the beginning of the dynamics at 10 K. During the later dynamics, hops overcoming the two large gaps (see density of excited states in the top panel in Figure 2) are infrequent, thus slowing the overall relaxation rate (the bottom panels in Figure 4). At 10 K we observe clear branching of the initial wavepacket into three peaks gradually raising after the system sequentially overcomes the gaps in is spectrum. These three subwavepackets are strongly overlapping in the 300 K case, where large conformational space sampling results in a much faster relaxation rate.

C. Analysis of Vibrational Dynamics. Since it is impossible to follow all vibrational degrees of freedom, even for a small molecule, we monitor the specific nuclear motions that are strongly coupled to the electronic degrees of freedom. Specifically, the bond length alternation (BLA) and torsion of the vinylene segment have been previously identified as the fast and slow nuclear coordinates, respectively.[28,32,64,98] Consequently, we first perform a simple analysis for distyrylbenzene by calculating the potential energy "slices" scanned along these nuclear coordinates. Potential energies for S_0 and S_1 states were computed using a single-point CEO calculation and various geometries created by specifying the particular angles and bond lengths simulteneously changed along the molecule. The resulting plots are provided in Figure 5.

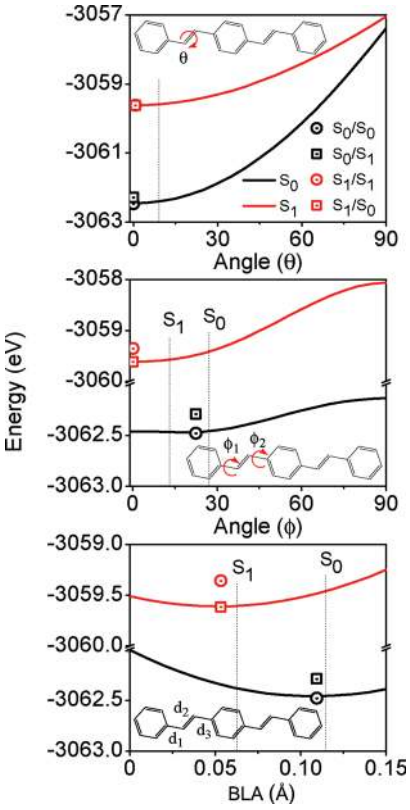

Figure 5. Potential energy surface slices for S_0 (black line) and S_1 (red line) states calculated by varying torsional angles and bond lengths. Circular and square points represent ground-state and lowest energy excited-state optimized geometries, respectively, using the conventional quantum-chemical notation single-point/optimization level. Dashed lines indicate the maximum values observed in our dynamics simulations. Top: Rotation around the double bond measured by torsional angle θ. Middle: Rotation around the single bond where both torsional angles ϕ_1 and ϕ_2 are scanned simultaneously. Bottom: Variation of bond length alternation (BLA) parameter.

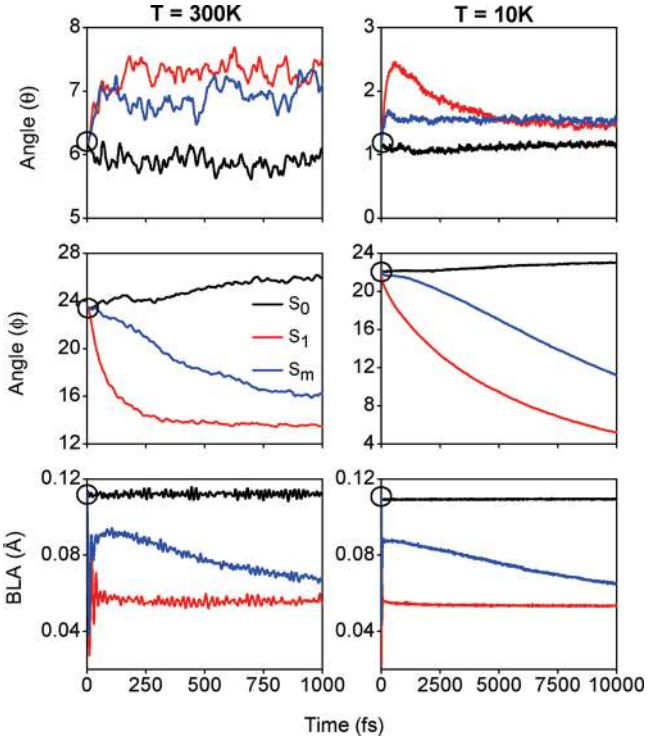

Figure 6. Variation of torsional angles (top and middle panels) and BLA parameter (bottom panel) averaged over the ensemble of trajectories for S_0 (black line), S_1 (red line), and S_m (blue line) dynamics simulations.

First, the rotation around the double bond was investigated (top panel in Figure 5). Starting from the S_0 (or S_1) *trans* geometry, the torsional angle around the double bond, θ, was scanned. Here $\theta = 0°$ corresponds to the *trans* configuration, and $\theta = 90°$ gives the configuration where the neighboring phenyl rings are orthogonal. Both the ground-state and excited-state optimized structures reveal a minimum potential energy near $\theta = 0°$ rotation so that the *trans* configuration is the most stable. However, the barrier for rotation is significantly descreased for the excited state suggesting that the double bond character is reduced following excitation allowing for a photoisomerization mechanism. Next, the rotation around the single bonds was analyzed by scanning the torsional angle from $\phi = 0°$ (coplanar arrangement of the phenyl rings) to $\phi = 90°$ (perpendicular arrangement of phenyl rings). The optimized geometry indicates that the stable S_0 configuration lies at $\phi = 22.4°$, while the S_1 configuration prefers the planar $\phi = 0°$ configuration (middle panel in Figure 5). In this case, the excited state has a larger rotational barrier indicating that the single bond gains the double bond character. Thus, upon S_1 photoexcitation, the distyrylbenzene is expected to relax to a planar conformation consistent with the predictions of a previous work.[29,32] Finally, we analyze the bond length alternation (BLA) parameter. The BLA is defined as the average difference between the C−C and C═C bond length $[\{(d_1 + d_3)/2\} - d_2)]$ of the vinylene segment (bottom panel in Figure 5). Scanning the BLA for the S_0 state reveals that the minimum potential energy for ground-state structure is at 0.11 Å in agreement with typical values for PPV systems.[29,114] For the excited state S_1, the minimum energy BLA is reduced to 0.06 Å. Thus, redistribution of the electronic density results in an increased rotation around the double bond and decreased rotation around the single bond, whereas bond length alternation concurrently decreases due to the more uniform bond length.

The average over 540 trajectories of the torsional angles, θ and ϕ, and the BLA parameter is plotted in Figure 6 for the simulated S_0, S_1, and S_m dynamics at room and low temperatures. In our discussion, we will be referring to the potential energy plots in Figure 5. Due to thermal fluctuations, the average C═C torsion in the ground state deviates from its optimal value (0°) to 1.7 and 6° at low and room temperatures, respectively. These angles stay the same along the S_0 trajectory. Upon excitation, electron density is removed from the double bond, thus lowering the barrier to rotation and allowing larger torsional angles to appear, as illustrated by an increase in torsional angle θ for both S_1 and S_m excited-state simulations (top panels in Figure 6). Again, C−C torsion fluctuates near the predicted equilibrium angle of $\phi = 22.4°$ in the S_0 simulation (middle panels in Figure 6). In contrast to θ, the torsional angle ϕ decreases upon excitation, and rotation around the single bond is hindered. After excitation, the molecule begins to planarize in an attempt to reach the planar S_1 minimum energy structure of $\phi = 0°$. Although the lowest-energy planar configuration is never realized, it is important to notice that the torsional angle decreases to $\phi = 14°$ and $\phi = 4°$ for the S_1 simulation at $T = 300$ K and $T = 10$ K, respectively.

The nonadiabatic S_m dynamics shows a less predictable behavior as the system is highly excited and has excessive vibrational energy. As the mA_g state decays to the $1B_u$ state, the S_m trajectory gradually converges to the S_1 result in both low- and high-temperature cases.

The average BLA for the S_0 dynamics fluctuates around 0.11 Å, with the room-temperature simulations showing more thermal fluctuations (bottom panels in Figure 6). This value coincides with the minimum potential energy BLA parameter from our BLA analysis in Figure 5. Similarly, the S_1 dynamics fluctuates near the predicted minimum energy BLA of 0.06 Å after a few periods of coherent BLA motion. This indicates a steep energy potential with respect to the BLA parameter. During the nonadiabatic S_m relaxation, the BLA adopts an intermediate value and gradually approaches the S_1 equilibrium value at rates concurrent with the population transfer to the $1B_u$ state for low- and high-temperature cases. Thus, the averaged BLA over the trajectories reflects an average value over several intermediate excited states.

IV. CONCLUSION

Knowledge of the excited-state potential energy surfaces and dynamics is needed to fully characterize nonadiabatic photochemical, photophysical, and spectroscopic processes. Theory, modeling, and simulation should match advances in the ultrafast nonlinear spectroscopy to interpret the data and extract relevant information on fundamental physical phenomena. However, even on the level of surface hopping methods, the nonadiabatic dynamics modeling requires significantly larger computational cost compared to the standard quantum-chemical calculations such as single-point electronic structure snapshot or geometry optimization. This necessity of propagating a large ensemble of trajectories practically rules out application of sophisticated excited-state ab initio methodologies to large molecular systems. The NA-ESMD framework[59,60] presented here provides a computationally accessible and reasonably accurate trade-off permitting description of photoinduced dynamics in large molecular systems consisting of hundreds of atoms on time scales of tens of picoseconds. The method uses actual excited-state potential energy surfaces calculated accounting for a minimal amount of many-body effects in the excited state (i.e., CIS or TDHF approximation). As a compromise, utilization of semiempirical model Hamiltonians delivers superb computational efficiency. While this description is fully adequate for organic molecules, the semiempirical parametrizations may be inaccurate for metals and heavy elements.

The NA-ESMD implementation of the FSSH switching procedure in Section II shows that an efficient MDQT modeling is possible only by combining advanced excited-state methodologies (e.g., Davidson diagonalization, analytic computation of state gradients, and nonadiabatic couplings) and optimal propagator techniques (e.g., synergy of Velocity Verlet and Runge−Kutta techniques used here to propagate classical and quantum dergrees of freedom). This approach can be directly transferred to a conceptually similar but more advanced TDDFT method, where treatment of nonadiabatic dynamics has been subject to recent investigations.[96−115] Our application of NA-ESMD code to simulate photoinduced dynamics in distyrylbenzene shows exhaustive insights into the fine details of the electronic structure and the relationship between dynamics, electronic coupling, and conformational changes within the system. The results agree well with available experimental data in terms of both electronic features and dynamical time scales, while providing a general understanding of the photoexcitation dynamics in the parent PPV materials. Applications of the NA-ESMD method to other molecular systems is a subject of our future studies.

AUTHOR INFORMATION

Corresponding Author
*E-mail: serg@lanl.gov.

ACKNOWLEDGMENT

T.N. and S.T. acknowledge support of the Center for Energy Efficient Materials (CEEM), an Energy Frontier Research Center funded by the U.S. Department of Energy (DOE), Office of Science, Office of Basic Energy Sciences (BES). This work was partially supported by CONICET, UNQ, NSF Grants CHE-0239120 and CHE-0808910. Los Alamos National Laboratory is operated by Los Alamos National Security, LLC, for the National Nuclear Security Administration of the U.S. Department of Energy under contract DE-AC52-06NA25396. We acknowledge support of the Center for Integrated Nanotechnology (CINT) and Center for Nonlinear Studies (CNLS).

REFERENCES

(1) Kamat, P. V. *J. Phys. Chem. C* **2007,** *111,* 2834–2860.
(2) Nozik, A. J. *Chem. Phys. Lett.* **2008,** *457,* 3–11.
(3) Schaller, R. D.; Sykora, M.; Pietryga, J. M.; Klimov, V. I. *Nano Lett.* **2006,** *6,* 424–429.
(4) Bang, J. H.; Kamat, P. V. *ACS Nano* **2009,** *3,* 1467–1476.
(5) Chua, L. L.; Zaumseil, J.; Chang, J. F.; Ou, E. C. W.; Ho, P. K. H.; Sirringhaus, H.; Friend, R. H. *Nature* **2005,** *434,* 194–199.
(6) Jia, Z.; Yi, C. *Small* **2007,** *3,* 1322.
(7) Klimov, V. I.; Ivanov, S. A.; Nanda, J.; Achermann, M.; Bezel, I.; McGuire, J. A.; Piryatinski, A. *Nature* **2007,** *447,* 441–446.
(8) Satishkumar, B. C.; Brown, L. O.; Gao, Y.; Wang, C. C.; Wang, H. L.; Doorn, S. K. *Nature Nanotechnol.* **2007,** *2,* 560.
(9) Thomas, S.; Joly, G.; Swager, T. *Chem. Rev.* **2007,** *107,* 1339–1386.
(10) Wang, D. L.; Gong, X.; Heeger, P. S.; Rininsland, F.; Bazan, G. C.; Heeger, A. J. *Proc. Natl. Acad. Sci. U.S.A.* **2002,** *99,* 49–53.
(11) Scholes, G. D. *ACS Nano* **2008,** *2,* 523–537.
(12) Scholes, G. D.; Rumbles, G. *Nature Mater.* **2006,** *5,* 683–696.
(13) Baldo, M. A.; Thompson, M. E.; Forrest, S. R. *Nature* **2000,** *403,* 750–753.
(14) Friend, R. H.; Gymer, R. W.; Holmes, A. B.; Burroughes, J. H.; Marks, R. N.; Taliani, C.; Bradley, D. D. C.; dos Santos, D. A.; Brédas, J. L.; Logdlund, M.; Salaneck, W. R. *Nature* **1999,** *397,* 121–128.
(15) Bredas, J. L.; Norton, J. E.; Cornil, J.; Coropceanu, V. *Acc. Chem. Res.* **2009,** *42,* 1691–1699.
(16) BarHaim, A.; Klafter, J.; Kopelman, R. *J. Am. Chem. Soc.* **1997,** *119,* 6197–6198.
(17) Kuroda, D. G.; Singh, C. P.; Peng, Z.; Kleiman, V. D. *Science* **2009,** *326,* 263–7.
(18) Granstrom, M.; Petritsch, K.; Arias, A. C.; Lux, A.; Andersson, M. R.; Friend, R. H. *Nature* **1998,** *395,* 257–260.
(19) Yu, G.; Gao, J.; Hummelen, J. C.; Wudl, F.; Heeger, A. J. *Science* **1995,** *270,* 1789–1791.
(20) Ho, P. K. H.; Kim, J. S.; Burroughes, J. H.; Becker, H.; Li, S. F. Y.; Brown, T. M.; Cacialli, F.; Friend, R. H. *Nature* **2000,** *404,* 481–484.
(21) Cao, Y.; Parker, I. D.; Yu, G.; Zhang, C.; Heeger, A. J. *Nature* **1999,** *397,* 414–417.
(22) Pei, Q. B.; Yu, G.; Zhang, C.; Yang, Y.; Heeger, A. J. *Science* **1995,** *269,* 1086–1088.

(23) Murphy, A.; Frechet, J. *Chem. Rev.* **2007,** *107,* 1066–1096.
(24) Yang, Y.; Heeger, A. J. *Nature* **1994,** *372,* 344–346.
(25) Lee, K.; Povlich, L. K.; Kim, J. *Analyst* **2010,** *135,* 2179–2189.
(26) Menard, E.; Meitl, M.; Sun, Y.; Park, J.-U.; Shir, D.-L.; Nam, Y.-S.; Jeon, S.; Rogers, J. *Chem. Rev.* **2007,** *107,* 1117–1160.
(27) Sirringhaus, H.; Kawase, T.; Friend, R. H.; Shimoda, T.; Inbasekaran, M.; Wu, W.; Woo, E. P. *Science* **2000,** *290,* 2123–2126.
(28) Karabunarliev, S.; Baumgarten, M.; Bittner, E.; Mullen, K. *J. Chem. Phys.* **2000,** *113,* 11372–11381.
(29) Tretiak, S.; Saxena, A.; Martin, R. L.; Bishop, A. R. *Phys. Rev. Lett.* **2002,** *89,* 097402.
(30) Bredas, J. L.; Street, G. B. *Acc. Chem. Res.* **1985,** *18,* 309–315.
(31) Niklasson, A. M. N.; Steneted, P.; Odell, A.; Bock, N.; Challacombe, M.; Tymczak, C. J.; Holmstrom, E.; Guishan, Z.; Weber, V. *J. Chem. Phys.* **2009,** *130,* 214109.
(32) Karabunarliev, S.; Baumgarten, M.; Mullen, K. *J. Phys. Chem. A* **2000,** *104,* 8236–8243.
(33) Molnar, F.; Ben-Nun, M.; Martinez, T. J.; Schulten, K. *J. Mol. Struct. Theochem* **2000,** *506,* 169–178.
(34) Franco, I.; Tretiak, S. *J. Am. Chem. Soc.* **2004,** *126,* 12130–12140.
(35) Gambetta, A.; Manzoni, C.; Menna, E.; Meneghetti, M.; Cerullo, G.; Lanzani, G.; Tretiak, S.; Piryatinski, A.; Saxena, A.; Martin, R. L.; Bishop, A. R. *Nature Phys.* **2006,** *2,* 515–20.
(36) Martinez, T. J. *Acc. Chem. Res.* **2006,** *39,* 119–126.
(37) Domcke, W.; Yarkony, D.; Koppel, H. *Conical intersections: electronic structure, dynamics and spectroscopy*; World Scientific Pub Co. Inc.: Singapore, 2004.
(38) Virshup, A. M.; Punwong, C.; Pogorelov, T. V.; Lindquist, B. A.; Ko, C.; Martinez, T. J. *J. Phys. Chem. B* **2009,** *113,* 3280–3291.
(39) Piryatinski, A.; Stepanov, M.; Tretiak, S.; Chernyak, V. *Phys. Rev. Lett.* **2005,** *95,* 223001.
(40) Gao, J. L.; Truhlar, D. G. *Annu. Rev. Phys. Chem.* **2002,** *53,* 467–505.
(41) Makri, N. *Annu. Rev. Phys. Chem.* **1999,** *50,* 167–191.
(42) Levine, B. G.; Martinez, T. J. *Annu. Rev. Phys. Chem.* **2007,** *58,* 613–634.
(43) Haobin, W.; Thoss, M. *J. Chem. Phys.* **2003,** *119,* 1289–1299.
(44) Manthe, U. *J. Chem. Phys.* **2008,** *128,* 164116.
(45) Worth, G. A. *J. Chem. Phys.* **2000,** *112,* 8322–8329.
(46) Tully, J. *J. Chem. Phys.* **1990,** *93,* 1061–1071.
(47) Drukker, K. *J. Comput. Phys.* **1999,** *153,* 225–272.
(48) Li, X.; Tully, J.; Schlegel, H.; Frisch, M. *J. Chem. Phys.* **2005,** *123,* 84106–1−7.
(49) Lan, Z.; Fabiano, E.; Thiel, W. *J. Phys. Chem. B* **2009,** *113,* 3548–3555.
(50) Fabiano, E.; Keal, T. W.; Thiel, W. *Chem. Phys.* **2008,** *349,* 334–347.
(51) Granucci, G.; Persico, M. *J. Chem. Phys.* **2007,** *126,* 134114.
(52) Granucci, G.; Persico, M.; Toniolo, A. *J. Chem. Phys.* **2001,** *114,* 10608.
(53) Singh, J.; Bittner, E. R.; Beljonne, D.; Scholes, G. D. *J. Chem. Phys.* **2009,** *131,* 194905.
(54) Prezhdo, O. V.; Duncan, W. R.; Prezhdo, V. V. *Prog. Surf. Sci.* **2009,** *84,* 30–68.
(55) Craig, C. F.; Duncan, W. R.; Prezhdo, O. V. *Phys. Rev. Lett.* **2005,** *95,* 163001.
(56) Duncan, W. R.; Prezhdo, O. V. *Annu. Rev. Phys. Chem.* **2007,** *58,* 143–184.
(57) Habenicht, B. F.; Prezhdo, O. V. *Nature Nanotechnol.* **2008,** *3,* 190–191.
(58) Allen, M. P.; Tildesley, D. J. *Computer Simulation of Liquids*; Oxford University Press: USA, 1990.
(59) Fernandez-Alberti, S.; Kleiman, V. D.; Tretiak, S.; Roitberg, A. E. *J. Phys. Chem. A* **2009,** *113,* 7535–7542.
(60) Fernandez-Alberti, S.; Kleiman, V. D.; Tretiak, S.; Roitberg, A. E. *J. Phys. Chem. Lett.* **2010,** *1,* 2699–2704.
(61) Lira-Cantu, M.; Krebs, F. *Sol. Energy Mater. Sol. Cells* **2006,** *90,* 2076–2086.
(62) Frolov, S. V.; Bao, Z.; Wohlgenannt, M.; Vardeny, Z. V. *Phys. Rev. Lett.* **2000,** *85,* 2196–2199.
(63) Cornil, J.; Beljonne, D.; Shuai, Z.; Hagler, T. W.; Campbell, I.; Bradley, D. D. C.; Brédas, J. L.; Spangler, C. W.; Mullen, K. *Chem. Phys. Lett.* **1995,** *247,* 425–432.
(64) Tretiak, S.; Mukamel, S. *Chem. Rev.* **2002,** *102,* 3171–3212.
(65) Mukamel, S.; Tretiak, S.; Wagersreiter, T.; Chernyak, V. *Science* **1997,** *277,* 781–787.
(66) Ridley, J.; Zerner, M. C. *Theor. Chim. Acta* **1973,** *32,* 111–134.
(67) Dewar, M. J. S.; Zoebisch, E. G.; Healy, E. F.; Stewart, J. J. P. *J. Am. Chem. Soc.* **1985,** *107,* 3902–3909.
(68) Thouless, D. J. *The Quantum Mechanics Of Many-Body Systems*; Academic Press: New York, 1972.
(69) Davidson, E. R. *Reduced Density Matrices in Quantum Chemistry*; Academic Press: New York, 1976.
(70) Davidson, E. R. *J. Comput. Phys.* **1975,** *17,* 87–94.
(71) Stratmann, R. E.; Scuseria, G. E.; Frisch, M. J. *J. Chem. Phys.* **1998,** *109,* 8218–8224.
(72) Chernyak, V.; Schulz, M. F.; Mukamel, S.; Tretiak, S.; Tsiper, E. V. *J. Chem. Phys.* **2000,** *113,* 36–43.
(73) Tretiak, S.; Isborn, C.; Niklasson, A.; Challacombe, M. *J. Chem. Phys.* **2009,** *130,* 054111.
(74) Rettrup, S. *J. Comput. Phys.* **1982,** *45,* 100–107.
(75) Ring, P.; Schuck, P. *The Nuclear Many-Body Problem*; Springer-Verlag: New York, 1980.
(76) Chernyak, V.; Mukamel, S. *J. Chem. Phys.* **1996,** *104,* 444–459.
(77) Szabo, A.; Ostlund, N. S. *Modern Quantum Chemistry: Introduction to Advanced Electronic Structure Theory*; McGraw-Hill: New York, 1989.
(78) Hirata, S.; Head-Gordon, M.; Bartlett, R. J. *J. Chem. Phys.* **1999,** *111,* 10774–10786.
(79) Tretiak, S.; Chernyak, V.; Mukamel, S. *J. Am. Chem. Soc.* **1997,** *119,* 11408–11419.
(80) Bazan, G. C.; Oldham, W. J.; Lachicotte, R. J.; Tretiak, S.; Chernyak, V.; Mukamel, S. *J. Am. Chem. Soc.* **1998,** *120,* 9188–9204.
(81) Tretiak, S.; Chernyak, V.; Mukamel, S. *Int. J. Quantum Chem.* **1998,** *70,* 711–727.
(82) Tretiak, S.; Chernyak, V.; Mukamel, S. *Phys. Rev. Lett.* **1996,** *77,* 4656–4659.
(83) Tretiak, S.; Chernyak, V.; Mukamel, S. *Chem. Phys. Lett.* **1998,** *287,* 75–82.
(84) Schulz, M.; Tretiak, S.; Chernyak, V.; Mukamel, S. *J. Am. Chem. Soc.* **2000,** *122,* 452–459.
(85) Tretiak, S.; Chernyak, V.; Mukamel, S. *J. Phys. Chem. B* **1998,** *102,* 3310–3315.
(86) Poliakov, E. Y.; Chernyak, V.; Tretiak, S.; Mukamel, S. *J. Chem. Phys.* **1999,** *110,* 8161–8175.
(87) Minami, T.; Tretiak, S.; Chernyak, V.; Mukamel, S. *J. Lumin.* **2000,** *87−9,* 115–118.
(88) Tretiak, S.; Middleton, C.; Chernyak, V.; Mukamel, S. *J. Phys. Chem. B* **2000,** *104,* 4519–4528.
(89) Tretiak, S.; Middleton, C.; Chernyak, V.; Mukamel, S. *J. Phys. Chem. B* **2000,** *104,* 9540–9553.
(90) Tretiak, S.; Chernyak, V. *J. Chem. Phys.* **2003,** *119,* 8809–8823.
(91) Tretiak, S.; Igumenshchev, K.; Chernyak, V. *Phys. Rev. B* **2005,** *71,* 33201.
(92) Igumenshchev, K. I.; Tretiak, S.; Chernyak, V. Y. *J. Chem. Phys.* **2007,** *127,* 1–10.
(93) Furche, F. *J. Chem. Phys.* **2001,** *114,* 5982–5992.
(94) Furche, F.; Ahlrichs, R. *J. Chem. Phys.* **2002,** *117,* 7433–7447.
(95) Tretiak, S.; Chernyak, V. *J. Chem. Phys.* **2003,** *119,* 8809–8823.
(96) Chernyak, V.; Mukamel, S. *J. Chem. Phys.* **2000,** *112,* 3572–3579.
(97) Tommasini, M.; Chernyak, V.; Mukamel, S. *Int. J. Quantum Chem.* **2001,** *85,* 225–238.

(98) Tretiak, S.; Saxena, A.; Martin, R. L.; Bishop, A. R. *Proc. Natl. Acad. Sci. U.S.A.* **2003,** *100*, 2185–2190.
(99) Moran, A. M.; Kelley, A. M.; Tretiak, S. *Chem. Phys. Lett.* **2003,** *367*, 293–307.
(100) Shreve, A. P.; Haroz, E. H.; Bachilo, S. M.; Weisman, R. B.; Tretiak, S.; Kilina, S.; Doorn, S. K. *Phys. Rev. Lett.* **2007,** *98*, 037405.
(101) van Gunsteren, W. F.; Berendsen, H. J. C. *Mol. Phys.* **1982,** *45*, 637.
(102) Swope, W. C.; Andersen, H. C.; Berens, P. H.; Wilson, K. R. *J. Chem. Phys.* **1982,** *76*, 637.
(103) Paterlini, M.; Ferguson, D. *Chem. Phys.* **1998,** *236*, 243–252.
(104) Press, W. H.; Teukolsky, S. A.; Vetterling, W. T.; Flannery, B. P. *Numerical Recipes in Fortran 77: the art of scientific computing*, 2nd ed.; Cambridge University Press: New York, 1996.
(105) Hammes-Schiffer, S.; Tully, J. C. *J. Chem. Phys.* **1994,** *101*, 4657–4667.
(106) Parandekar, P. V.; Tully, J. C. *J. Chem. Phys.* **2005,** *122*, 094102.
(107) Hull, T. E.; Enright, W.; Jackson, K. *User's guide for DVERK - A subroutine for solving non-stiff ODEs*; Technical Report 100, Department of Computer Science: University of Toronto: Canada, 1976.
(108) *IMSL MATH/LIBRARY Special Functions*; Visual Numerics, Inc.: Houston, TX 77042, USA.
(109) Pittner, J.; Lischka, H.; Barbatti, M. *Chem. Phys.* **2007,** *356*, 147–152.
(110) Chandross, M.; Mazumdar, S. *Phys. Rev. B* **1997,** *55*, 1497–1504.
(111) Baraldi, I.; Ginocchietti, G.; Mazzucato, U.; Spalletti, A. *Chem. Phys.* **2007,** *337*, 168–176.
(112) Brazovskii, S.; Kirova, N.; Bishop, A. R.; Klimov, V.; McBranch, D.; Barashkov, N. N.; Ferraris, J. P. *Opt. Mater.* **1998,** *9*, 472–479.
(113) Lukes, V.; Solc, R.; Barbatti, M.; Lischka, H.; Kauffmann, H.-F. *J. Theor. Comput. Chem.* **2010,** *9*, 249–263.
(114) Fu, Y.; Shen, W.; Li, M. *Polymer* **2008,** *49*, 2614.
(115) Send, R.; Furche, F. *J. Chem. Phys.* **2010,** *132*, No. 044107.